*Proceedings of the*
*Annual Stability Conference*
*Structural Stability Research Council*
*Louisville, Kentucky, April 13-16, 2021*

# On the combination of shell and GBT-based beam finite elements

David Manta[1], Rodrigo Gonçalves[2], Dinar Camotim[3]

## Abstract

This paper proposes a quite general and computationally efficient approach to model thin-walled members and frames with complex geometries (including tapered and perforated members). The approach consists of combining shell and GBT-based (beam) finite elements, using each element type where it is most advantageous: (i) shell elements are assigned to the plastic and geometrically complex zones, whereas (ii) GBT elements are employed in the prismatic and elastic zones. To illustrate the capabilities and potential of the proposed approach, several numerical examples are presented, involving linear (first-order) static, bifurcation (linear stability), undamped free vibration, dynamic and first-order plastic zone analyses. The examples analyzed deal with (i) members with tapered segments, (ii) perforated members and (iii) complex beam-column assemblies. For validation and comparison purposes, full shell finite element solutions are provided, showing that an excellent match is obtained in all cases.

## 1. Introduction

It is widely accepted that, due to its modal decomposition features, Generalized Beam Theory (GBT) constitutes an efficient tool to analyze thin-walled prismatic members undergoing cross-section in-plane and out-of-plane (warping) deformation: the member deformed configuration is expressed as a linear combination of so-called "cross-section deformation modes", which have a clear and hierarchical physical/structural nature. GBT is most efficient in the context of linear, bifurcation (linear stability) and undamped free vibration analyses, where the inclusion of just a few deformation modes leads to very accurate solutions. Moreover, in such cases, it is often possible to derive analytical or semi-analytical solutions. GBT was initially developed by Schardt (1966, 1989) (see http://vtb.info for related bibliography) and was subsequently developed by several researchers, namely the Lisbon-based research group (see http://www.civil.ist.utl.pt/gbt for a list of publications).

As already mentioned, GBT is essentially a prismatic bar theory, but some efforts have been undertaken to extend its domain of application to other cases. Formulations are now available for moderately tapered members (Nedelcu 2010), conical shells (Nedelcu 2011, Muresan et al. 2019)

---

[1] PhD Student, CERIS and Universidade Nova de Lisboa, Portugal <d.manta@campus.fct.unl.pt> >

[2] Associate Professor, CERIS and Universidade Nova de Lisboa, Portugal <rodrigo.goncalves@fct.unl.pt> >

[3] Full Professor, CERIS, Instituto Superior Técnico, Universidade de Lisboa, Portugal <dcamotim@civil.ist.utl.pt>

and perforated members (Cai & Moen 2016), the latter at the expense of a refined cross-section discretisation and considering only membrane longitudinal normal pre-buckling stresses. A more general approach to handle perforated members (members with holes), discrete thickness variation, plasticity and geometrical non-linearity was proposed by Gonçalves & Camotim (2017), using non-orthogonal deformation modes to tackle complex geometries and improve the computational efficiency (the orthogonal mode participations are retrieved through post-processing). It is also worth noting that a linear formulation for members with circular axis was proposed by Peres et al. (2016, 2018) and that frames can also be analyzed, using carefully chosen constraints at the nodes (Basaglia et al. 2008, 2009, 2013; Camotim & Basaglia 2013).

GBT has also been applied to non-linear materials, most efficiently for plastic bifurcation problems (Gonçalves & Camotim 2004, Gonçalves et al. 2010). For tracing non-linear equilibrium paths, although the modal decomposition features of GBT are still enlightening, the computational efficiency is partially lost because (i) many deformation modes need to be included in the analysis, leading to DOF numbers comparable to those required by similarly accurate shell element models, and (ii) large and dense element stiffness matrices are obtained. This obvious drawback led to the development of several circumventing strategies for steel plasticity and concrete cracking/crushing: the use of (i) stress constraints that enable reducing the number of deformation modes (Gonçalves & Camotim 2011, Henriques et al. 2015, 2016, 2020) and (ii) shell-like stress resultant yield functions to reduce the number of modes and avoid the expensive through-thickness numerical integration (Gonçalves & Camotim 2011, 2012). As mentioned earlier, the approach proposed by Gonçalves & Camotim (2017) can also handle physical and materially non-linearity quite efficiently, but it still lacks the generality of shell finite elements.

In this paper, an alternative, general and efficient approach is proposed, which combines genuine shell and GBT-based (beam) finite elements, with each element type being employed where is is most effective: (i) shell elements in the plastic and/or geometrically complex zones (tapered parts, holes, joints, etc.), and (ii) GBT elements in the prismatic and elastic zones. This approach makes it possible to include only a small number of deformation modes in the GBT elements without sacrificing accuracy, since the zones whose correct GBT modeling would require many deformation modes are instead (and more efficiently) handled using shell elements. To illustrate the capabilities and potential of the proposed approach, several numerical examples are presented, involving linear (first-order) static, bifurcation (linear stability), undamped free vibration, dynamic and first-order plastic zone analyses. These examples deal with (i) members with tapered segments, (ii) perforated members and (iii) frames with complex beam-column assemblies. For validation and comparison purposes, full shell finite element solutions are provided, showing that an excellent match is observed in all cases.

Concerning the notation, scalars are represented by *italic* letters and vectors/matrices by **bold** letters. Identity matrices are displayed as $\mathbf{1}$ and null matrices or vectors by $\mathbf{0}$ (their dimensions are defined implicitly in the formulas they appear in). The standard Euclidean inner product between two vectors of arbitrary dimension $\boldsymbol{a}$ and $\boldsymbol{b}$ is written as $\boldsymbol{a} \cdot \boldsymbol{b}$, a derivative is represented by a subscript comma (e.g., $f_{,a} = \partial f / \partial a$), although time derivatives are identified by a dot (i.e., $\dot{f} = \partial f / \partial t$). Moreover, a virtual variation is denoted by $\delta$ and an incremental/iterative variation by $\Delta$. Finally, $h$ is the shell/wall thickness and the membrane/bending/through-thickness shear terms are identified by indices $M$, $B$ and $S$, respectively.

## 2. Brief overview of the adopted shell and GBT-based finite elements

First, the fundamental equilibrium equations and their linearization are presented. Using virtual work, written in terms of Green-Lagrange strains $\boldsymbol{E}$ and second Piola-Kirchhoff stresses $\boldsymbol{S}$ in a Voigt-like notation, one has

$$\delta W = -\int_V \left(\delta \boldsymbol{U} \cdot \rho \ddot{\boldsymbol{U}} + \delta \boldsymbol{E} \cdot \boldsymbol{S}\right) \mathrm{d}V + \int_\Omega \delta \overline{\boldsymbol{U}} \cdot \boldsymbol{q} \, \mathrm{d}\Omega \ = 0, \tag{1}$$

Where (i) $\rho$, $V$ and $\Omega$ are the thin-walled member mass density, volume and mid-surface, respectively, at the initial configuration, (ii) $\boldsymbol{U}$ is the displacement vector and (iii) it is assumed that the external loads $\boldsymbol{q}$ are applied only at the element mid-surface, where $\overline{\boldsymbol{U}}$ are the work-conjugate mid-surface displacements. For a linear material, $\boldsymbol{S} = \boldsymbol{C}\boldsymbol{E}$, where $\boldsymbol{C}$ is the constitutive matrix. For elastoplastic materials, the incremental form of the constitutive equations reads

$$\mathrm{d}\boldsymbol{S} = \boldsymbol{C}_{ct} \mathrm{d}\boldsymbol{E}, \tag{2}$$

where $\boldsymbol{C}_{ct}$ is the tangent elastoplastic constitutive matrix consistent with the stress update algorithm employed — the backward Euler return scheme is employed in this paper (Simo & Taylor 1985). For non-linear problems, an incremental/iterative scheme must be adopted and the linearization of Eq. (1) is required to obtain the element tangent stiffness matrix and incremental/iterative nodal force vector, yielding

$$\Delta\delta W = -\int_V \left(\delta \boldsymbol{U} \cdot \rho \Delta\ddot{\boldsymbol{U}} + \Delta\delta \boldsymbol{E} \cdot \boldsymbol{S} + \delta \boldsymbol{E} \cdot \Delta\boldsymbol{S}\right) \mathrm{d}V + \int_\Omega \delta \overline{\boldsymbol{U}} \cdot \Delta\boldsymbol{q} \, \mathrm{d}\Omega. \tag{3}$$

The previous formulas will be particularized next for the analyses considered in this paper.

In geometrically linear static analysis, the Green-Lagrange strains become small strains $\boldsymbol{\varepsilon}$, which are work-conjugate to the stress vector $\boldsymbol{\sigma}$, and the virtual work reads

$$\delta W = -\int_V \delta \boldsymbol{\varepsilon} \cdot \boldsymbol{\sigma} \, \mathrm{d}V + \int_\Omega \delta \overline{\boldsymbol{U}} \cdot \boldsymbol{q} \, \mathrm{d}\Omega. \tag{4}$$

In the elastic case, $\boldsymbol{\sigma} = \boldsymbol{C}\boldsymbol{\varepsilon}$ and the first term leads to the element linear stiffness matrix, as no linearization is required, whereas the second term yields the element nodal force vector. For elastoplastic materials, Eq. (2) applies and the linearization of Eq. (4) becomes

$$\Delta\delta W = -\int_V \delta \boldsymbol{\varepsilon} \cdot \boldsymbol{C}_{ct} \Delta\boldsymbol{\varepsilon} \, \mathrm{d}V + \int_\Omega \delta \overline{\boldsymbol{U}} \cdot \Delta\boldsymbol{q} \, \mathrm{d}\Omega. \tag{5}$$

The first term leads to the element tangent stiffness matrix and the second term corresponds to the element incremental/iterative nodal force vector.

In linear stability analysis, a preliminary linear analysis must be performed to retrieve the pre-buckling stresses. Since this paper concerns thin-walled members, only the membrane stresses $\boldsymbol{S}^M$ are retained. The linearization of Eq. (3) at the initial configuration yields

$$\Delta\delta W(\boldsymbol{U}=\boldsymbol{0},\lambda) = -\int_V (\delta\boldsymbol{\varepsilon}\cdot\boldsymbol{C}\Delta\boldsymbol{\varepsilon} + \Delta\delta\boldsymbol{E}\cdot\lambda\boldsymbol{S}^M)\,\mathrm{d}V, \tag{6}$$

where $\lambda$ is the loading multiplier ($\boldsymbol{S}^M$ is calculated for $\lambda = 1$). The first and second terms in Eq. (6) lead to the finite element linear and geometric stiffness matrices, respectively. As usual, the bifurcation loads and corresponding buckling modes are obtained by the condition of singularity of the total stiffness matrix.

In geometrically and materially linear dynamic analysis, Eq. (1) readily yields

$$\delta W = -\int_V \left(\delta\boldsymbol{U}\cdot\rho\ddot{\boldsymbol{U}} + \delta\boldsymbol{\varepsilon}\cdot\boldsymbol{C}\boldsymbol{\varepsilon}\right)\mathrm{d}V + \int_\Omega \delta\bar{\boldsymbol{U}}\cdot\boldsymbol{q}\,\mathrm{d}\Omega = 0. \tag{7}$$

and is solved using Newmark's method. Finally, the natural frequencies and associated vibration modes are obtained from the homogeneous form of Eq. (7), whose time solution is sinusoidal with an angular frequency $\omega$, leading to the standard eigenvalue problem

$$\delta W = -\int_V \delta\boldsymbol{\varepsilon}\cdot\boldsymbol{C}\boldsymbol{\varepsilon}\,\mathrm{d}V + \omega^2\int_V \delta\boldsymbol{U}\cdot\rho\boldsymbol{U}\,\mathrm{d}V = 0, \tag{8}$$

where the second integral leads to the mass matrix.

The finite element procedures were implemented in MATLAB (2010). A post-processing module was included to visualize the deformed configurations and the vibration/buckling mode shapes.

### *2.1 The MITC-4 shell finite element*

As done by Manta et al. (2020, 2021), the shell element employed in this work is the 4-node Reissner-Mindlin Mixed Interpolation of Tensorial Components (MITC-4) element (Bathe 1996, Bathe & Dvorkin 1985), even if any other shell element could have been used. Fig. 1 displays three reference systems: (i) the global Cartesian system $(X, Y, Z)$, (ii) the element Cartesian local axes $(x, y, z)$, where $x$ is aligned with one of the lateral faces and $z$ defines the through-thickness direction (the shell is initially flat), and (iii) a convected frame $(r, s, t)$, where $t$ coincides with the local $z$ axis. With the mid-surface displacements $u$, $v$, $w$ and the rotations $\theta_x$, $\theta_y$ along the local axes, the element displacement field $\boldsymbol{U}$ can be written as

$$\boldsymbol{U}(x,y,z) = \begin{bmatrix} U_x \\ U_y \\ U_z \end{bmatrix} = \begin{bmatrix} u(x,y) + z\theta_y(x,y) \\ v(x,y) - z\theta_x(x,y) \\ w(x,y) \end{bmatrix}. \tag{9}$$

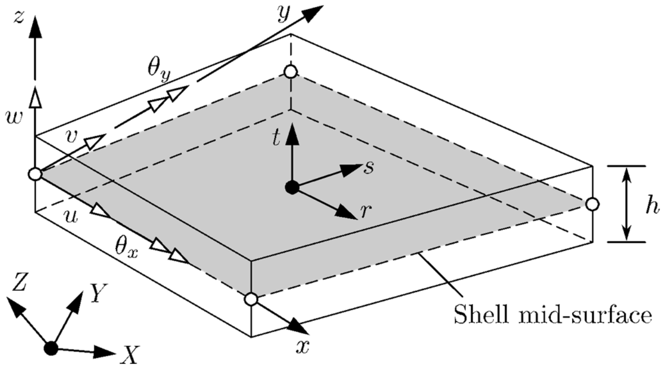

Figure 1: MITC-4 reference systems and displacement components.

The Green-Lagrange strains are subdivided into membrane ($M$), bending ($B$) and through-thickness shear ($S$) components, although only the non-linear part of $\boldsymbol{E}^M$ is retained, with

$$\boldsymbol{E}^M = \begin{bmatrix} E_{xx}^M \\ E_{yy}^M \\ 2E_{xy}^M \end{bmatrix} = \begin{bmatrix} u_{,x} \\ v_{,y} \\ u_{,y} + v_{,x} \end{bmatrix} + \frac{1}{2} \begin{bmatrix} \overline{\boldsymbol{U}}_{,x} \cdot \overline{\boldsymbol{U}}_{,x} \\ \overline{\boldsymbol{U}}_{,y} \cdot \overline{\boldsymbol{U}}_{,y} \\ 2\overline{\boldsymbol{U}}_{,x} \cdot \overline{\boldsymbol{U}}_{,y} \end{bmatrix}, \tag{10}$$

$$\boldsymbol{E}^B = \begin{bmatrix} E_{xx}^B \\ E_{yy}^B \\ 2E_{xy}^B \end{bmatrix} = z \begin{bmatrix} \theta_{y,x} \\ -\theta_{y,x} \\ \theta_{y,y} - \theta_{x,x} \end{bmatrix}, \tag{11}$$

$$\boldsymbol{E}^S = \begin{bmatrix} 2E_{xz} \\ 2E_{yz} \end{bmatrix} = \begin{bmatrix} w_{,x} + \theta_y \\ w_{,y} - \theta_x \end{bmatrix}, \tag{12}$$

where $\overline{\boldsymbol{U}}^T = [u \quad v \quad w]$ is the mid-surface displacement vector. In geometrically linear or bifurcation analyses, no membrane locking occurs (the element is initially flat), but shear locking may occur and is resolved by re-interpolating the covariant through-thickness shear strains from their values at the so-called “tying points” (Bathe 1996). The finite element is obtained by interpolating the mid-surface displacements and rotations using linear functions and following a standard isoparametric approach. The independent kinematic variables are collected in vector

$$\boldsymbol{\phi}^T = [u \quad v \quad w \quad \theta_x \quad \theta_y], \tag{13}$$

and the interpolation is $\boldsymbol{\phi} = \boldsymbol{\Psi d}$, where $\boldsymbol{\Psi}$ is a matrix containing the interpolation functions

$$\boldsymbol{\Psi}^T = \begin{bmatrix} \boldsymbol{\psi}_u^T & \boldsymbol{\psi}_v^T & \boldsymbol{\psi}_w^T & \boldsymbol{\psi}_{\theta_x}^T & \boldsymbol{\psi}_{\theta_y}^T \end{bmatrix}, \tag{14}$$

where $\boldsymbol{\psi}_{(\cdot)}$ are sub-matrices matching the components of the vector of nodal unknowns

$$\boldsymbol{d}^T = \begin{bmatrix} u_1 & v_1 & w_1 & (\theta_x)_1 & (\theta_y)_1 & \cdots & u_4 & v_4 & w_4 & (\theta_x)_4 & (\theta_y)_4 \end{bmatrix}, \tag{15}$$

leading to a 20 DOF element.

In first-order static analysis and recalling Eq. (4), the finite element out-of-balance force vector $\boldsymbol{g_e}$ is given by

$$\boldsymbol{g_e} = \int_V \begin{bmatrix} \boldsymbol{B}_M + \boldsymbol{B}_B \\ \boldsymbol{B}_S \end{bmatrix}^T \boldsymbol{\sigma}\,\mathrm{d}V - \int_\Omega \bar{\boldsymbol{\Psi}}_U^T \boldsymbol{q}\,\mathrm{d}\Omega, \tag{16}$$

where $\bar{\boldsymbol{\Psi}}_U^T = [\boldsymbol{\psi}_u^T \quad \boldsymbol{\psi}_v^T \quad \boldsymbol{\psi}_w^T \quad \mathbf{0} \quad \mathbf{0}]$ interpolates the mid-surface displacements (i.e. $\bar{\boldsymbol{U}} = \bar{\boldsymbol{\Psi}}_U \boldsymbol{d}$) and the interested reader can find the expressions of the strain-displacement matrices $\boldsymbol{B}_M$, $\boldsymbol{B}_B$ in Manta et al. (2020) and $\boldsymbol{B}_S$ in Bathe & Dvorkin (1985). In addition, the element tangent stiffness matrix $\boldsymbol{K}_e$ and the incremental load vector $\Delta\boldsymbol{f}_e$ are obtained from Eq. (5), reading

$$\boldsymbol{K}_e = \int_V \begin{bmatrix} \boldsymbol{B}_M + \boldsymbol{B}_B \\ \boldsymbol{B}_S \end{bmatrix}^T \boldsymbol{C}_{ct} \begin{bmatrix} \boldsymbol{B}_M + \boldsymbol{B}_B \\ \boldsymbol{B}_S \end{bmatrix} \mathrm{d}V, \tag{17}$$

$$\Delta\boldsymbol{f}_e = \int_\Omega \bar{\boldsymbol{\Psi}}_U^T\, \Delta\boldsymbol{q}\,\mathrm{d}\Omega. \tag{18}$$

For an elastic material, a plane stress state is assumed ($\sigma_{zz}$ =0), and a St. Venant-Kirchhoff material law is adopted, with

$$\boldsymbol{C}_{ct} = \boldsymbol{C} = \begin{bmatrix} \frac{E}{1-\nu^2} & \frac{\nu E}{1-\nu^2} & 0 & 0 & 0 \\ \frac{\nu E}{1-\nu^2} & \frac{E}{1-\nu^2} & 0 & 0 & 0 \\ 0 & 0 & G & 0 & 0 \\ 0 & 0 & 0 & G & 0 \\ 0 & 0 & 0 & 0 & G \end{bmatrix}, \tag{19}$$

where $E$ and $G$ are Young's and shear moduli and $\nu$ is Poisson's ratio. For an elastoplastic material, small-strain $J_2$ plasticity is implemented, with an associated flow rule and no hardening. The yield function is given by

$$f = \sqrt{3/2}\,\|\mathrm{dev}(\boldsymbol{\sigma})\| - \sigma_0, \tag{20}$$

where $\|\mathrm{dev}(\boldsymbol{\sigma})\|$ is the norm of the deviatoric stresses and $\sigma_0$ is the uniaxial yield stress. At the end of each iteration, for each integration point, stresses falling outside the yield surface are updated using the standard backward-Euler return mapping algorithm under the $\sigma_{zz}$ =0 constraint. The quadratic convergence of the iterative solution is ensured by using the consistent tangent constitutive operator $\boldsymbol{C}_{ct}$ (see, e.g., Simo & Taylor 1985, Ritto-Corrêa & Camotim 2001).

In linear stability analysis, the element geometric matrix is obtained from the second term of Eq. (6), leading to

$$\boldsymbol{G}_e = \lambda \int_V S_{xx}^M \bar{\boldsymbol{B}}_{xx}^T \bar{\boldsymbol{B}}_{xx} + S_{yy}^M \bar{\boldsymbol{B}}_{yy}^T \bar{\boldsymbol{B}}_{yy} + S_{xy}^M \left(\bar{\boldsymbol{B}}_{xx}^T \bar{\boldsymbol{B}}_{yy} + \bar{\boldsymbol{B}}_{yy}^T \bar{\boldsymbol{B}}_{xx}\right) \mathrm{d}V, \tag{21}$$

where the auxiliary matrices $\bar{\boldsymbol{B}}_{xx}$ and $\bar{\boldsymbol{B}}_{yy}$ are provided in Manta et al. (2020).

Finally, in the dynamic case the element mass matrix can be obtained from Eq. (8), reading

$$\boldsymbol{M}_e = \int_{\Omega} \rho h \bar{\boldsymbol{\Psi}}_U^T \bar{\boldsymbol{\Psi}}_U + \frac{\rho h^3}{12} \bar{\boldsymbol{\Psi}}_\theta^T \bar{\boldsymbol{\Psi}}_\theta \mathrm{d}\Omega, \tag{22}$$

where the auxiliary matrix $\bar{\boldsymbol{\Psi}}_\theta^T = \begin{bmatrix} \boldsymbol{0} & \boldsymbol{0} & \boldsymbol{0} & \boldsymbol{\psi}_{\theta_x}^T & \boldsymbol{\psi}_{\theta_y}^T \end{bmatrix}$ interpolates the mid-surface rotations.

For the computation of all matrices and vectors, numerical integration is performed using a 2 × 2 Gauss point grid along the shell mid-surface. Along the thickness direction, (i) analytical integration is performed in the elastic case and (ii) 6 Gauss points are used in the elastoplastic case, to capture accurately the plasticity spreading.

### *2.2 The GBT-based finite element*

The GBT element employed essentially corresponds to that proposed by Gonçalves & Camotim (2012), although (i) geometrical imperfections are discarded, (ii) some simplifications are introduced to the membrane stress and strain fields (discussed next), (iii) a linear elastic material is always assumed and, in linear stability analysis, (iv) only the non-linear longitudinal membrane strains are considered (an acceptable simplification in slender bars).

Fig. 2 shows two walls of an arbitrary prismatic thin-walled bar, the global Cartesian axes $(X, Y, Z)$, where $X$ defines the member longitudinal axis, and the local Cartesian axes for each wall $(x, y, z)$, defining the member axis, wall mid-line and thickness directions, respectively. In the classic GBT approach, Kirchhoff's thin plate assumption is adopted and the displacement vector for each wall is expressed, in the local axes, as

$$\boldsymbol{U}(x, y, z) = \begin{bmatrix} U_x \\ U_y \\ U_z \end{bmatrix} = \begin{bmatrix} (\bar{\boldsymbol{u}} - z\bar{\boldsymbol{w}}) \cdot \boldsymbol{\phi}_{,x} \\ (\bar{\boldsymbol{v}} - z\bar{\boldsymbol{w}}_{,y}) \cdot \boldsymbol{\phi} \\ \bar{\boldsymbol{w}} \cdot \boldsymbol{\phi} \end{bmatrix}, \tag{23}$$

where $\bar{\boldsymbol{u}}(y)$, $\bar{\boldsymbol{v}}(y)$, $\bar{\boldsymbol{w}}(y)$ are column vectors containing the displacement components of the so-called "cross-section deformation modes" along $x$, $y$ and $z$, respectively, and $\boldsymbol{\phi}(x)$ is a column vector collecting the corresponding amplitude functions (the problem unknowns). The deformation modes are obtained from a "GBT cross-section analysis", which was described in detail by Gonçalves et al. (2014) and Bebiano et al. (2015), and implemented in the GBTUL program (Bebiano et al. 2018), available for free download at www.civil.ist.utl.pt/gbt. This cross-section analysis is based on a cross-section discretization into "natural" nodes, located at wall mid-line intersections and free ends, and "intermediate nodes", arbitrarily located within each wall mid-line.

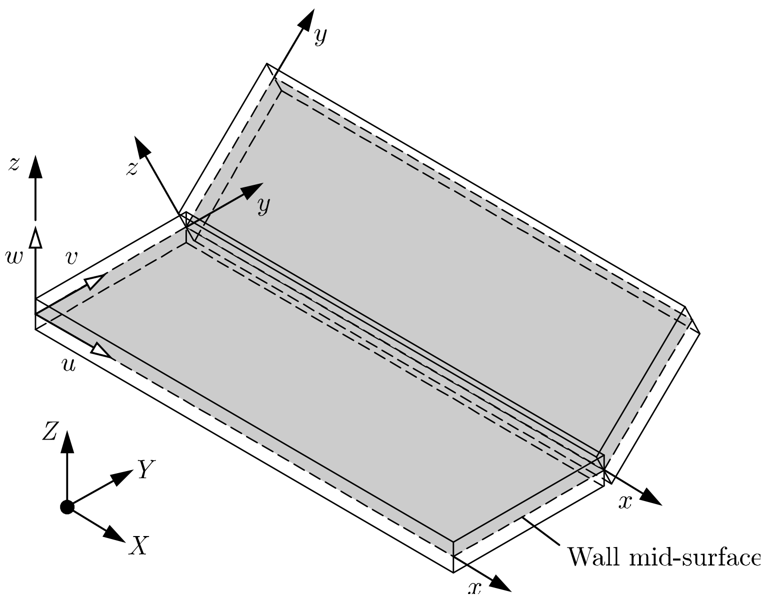

Figure 2: Global/local coordinate systems and local displacement components for two walls of an arbitrary thin-walled member.

In the geometrically linear case, the non-null small strain components read

$$\boldsymbol{\varepsilon} = \begin{bmatrix} \varepsilon_{xx} \\ \varepsilon_{yy} \\ \gamma_{xy} \end{bmatrix} = \begin{bmatrix} (\bar{\boldsymbol{u}} - z\bar{\boldsymbol{w}}) \cdot \boldsymbol{\phi}_{,xx} \\ \left(\bar{\boldsymbol{v}}_{,y} - z\bar{\boldsymbol{w}}_{,yy}\right) \cdot \boldsymbol{\phi} \\ \left(\bar{\boldsymbol{u}}_{,y} + \bar{\boldsymbol{v}} - 2z\bar{\boldsymbol{w}}_{,y}\right) \cdot \boldsymbol{\phi}_{,x} \end{bmatrix}, \tag{24}$$

where the membrane and bending terms are constant and linear along $z$, respectively. Recalling that one aims at modeling (i) complex zones with shell elements and (ii) the remaining (prismatic) zones with GBT elements that include just a few deformation modes, as already mentioned, simplifications are introduced to the membrane stress and strain fields, to enhance the computational efficiency without compromising accuracy: $\varepsilon_{yy}^M = \sigma_{xy}^M = 0$ and $\gamma_{xy}^M = \sigma_{xy}^M = 0$. With these constraints, only two deformation mode sets are obtained: (i) the so-called natural Vlasov modes (axial extension, bending, torsion for open sections and distortional modes) and (ii) local-plate modes. In closed sections, the torsional mode involves membrane shear strains and therefore the $\gamma_{xy}^M = 0$ constraint must be relaxed.

As mentioned earlier, in linear stability analysis only the non-linear longitudinal membrane strains are considered, meaning that the Green-Lagrange strains read $\boldsymbol{E}^T = \left[E_{xx}\ \varepsilon_{yy}\ \gamma_{xy}\right]^T$, with

$$\boldsymbol{E}_{xx}^M = \boldsymbol{\varepsilon}_{xx} + \frac{1}{2}\left(\boldsymbol{\phi}_{,x}^T(\bar{\boldsymbol{v}}\bar{\boldsymbol{v}}^T + \bar{\boldsymbol{w}}\bar{\boldsymbol{w}}^T)\boldsymbol{\phi}_{,x} + \boldsymbol{\phi}_{,xx}^T\bar{\boldsymbol{u}}\bar{\boldsymbol{u}}^T\boldsymbol{\phi}_{,xx}\right). \tag{25}$$

The term $\bar{\boldsymbol{u}}\bar{\boldsymbol{u}}^T$ is also discarded without significant loss of accuracy (see Gonçalves et al. 2010).

A plane stress state is assumed, with $\boldsymbol{S}^T = \left[S_{xx}\ S_{yy}\ S_{xy}\right]^T$. Due to the $\varepsilon_{yy}^M = 0$ constraint, the membrane and bending stress components are separated in order to avoid over-stiff solutions, with

$$\boldsymbol{S}^M = \boldsymbol{C}^M \boldsymbol{E}^M, \quad \boldsymbol{S}^B = \boldsymbol{C}^B \boldsymbol{E}^B, \tag{26}$$

$$\boldsymbol{C}^M = \begin{bmatrix} E & 0 & 0 \\ 0 & 0 & 0 \\ 0 & 0 & 0 \end{bmatrix}, \quad \boldsymbol{C}^B = \frac{E}{1-\nu^2} \begin{bmatrix} 1 & \nu & 0 \\ \nu & 1 & 0 \\ 0 & 0 & \dfrac{1-\nu}{2} \end{bmatrix}. \tag{27}$$

The finite element is obtained by interpolating the amplitude functions using Hermite cubic polynomials for all deformation modes except those involving only warping (e.g., axial extension), in which case quadratic hierarchical Lagrange functions are employed. Like for the shell elements, the interpolation is given by $\boldsymbol{\phi} = \boldsymbol{\Psi d}$, where matrix $\boldsymbol{\Psi}$ contains the interpolation functions and $\boldsymbol{d}$ is the vector of nodal unknowns.

In linear static analysis, from Eq. (4), the element stiffness matrix reads

$$\boldsymbol{K}_e = \int_L \begin{bmatrix} \boldsymbol{\Psi} \\ \boldsymbol{\Psi}_{,x} \\ \boldsymbol{\Psi}_{,xx} \end{bmatrix}^T \begin{bmatrix} \mathbf{B} & \mathbf{0} & \mathbf{D}_2 \\ \mathbf{0} & \mathbf{D}_1 & \mathbf{0} \\ \mathbf{D}_2^T & \mathbf{0} & \mathbf{C} \end{bmatrix} \begin{bmatrix} \boldsymbol{\Psi} \\ \boldsymbol{\Psi}_{,x} \\ \boldsymbol{\Psi}_{,xx} \end{bmatrix} \mathrm{d}x, \tag{28}$$

where $L$ is the finite element length and the GBT modal matrices are given by ($S$ is the cross-section mid-line)

$$\begin{gathered} \mathbf{B} = \int_S \frac{Eh^3}{12(1-\nu^2)} \overline{\boldsymbol{w}}_{,yy} \overline{\boldsymbol{w}}_{,yy}^T \, \mathrm{d}y, \quad \mathbf{C} = \int_S Eh \overline{\boldsymbol{u}} \overline{\boldsymbol{u}}^T + \frac{Eh^3}{12(1-\nu^2)} \overline{\boldsymbol{w}} \overline{\boldsymbol{w}}^T \, \mathrm{d}y, \\ \mathbf{D}_1 = \int_S \frac{Gh^3}{3} \overline{\boldsymbol{w}}_{,y} \overline{\boldsymbol{w}}_{,y}^T \, \mathrm{d}y, \quad \mathbf{D}_2 = \int_S \frac{\nu Eh^3}{12(1-\nu^2)} \overline{\boldsymbol{w}}_{,yy} \overline{\boldsymbol{w}}^T \, \mathrm{d}y, \end{gathered} \tag{29}$$

In linear stability analysis, from Eq. (6), the element geometric stiffness matrix reads

$$\boldsymbol{G}_e = \lambda \int_L \int_S h S_{xx}^M \boldsymbol{\Psi}_{,x}^T (\overline{\boldsymbol{v}} \overline{\boldsymbol{v}}^T + \overline{\boldsymbol{w}} \overline{\boldsymbol{w}}^T) \boldsymbol{\Psi}_{,x} \, \mathrm{d}y \, \mathrm{d}x \,. \tag{30}$$

For the dynamic case, the mass matrix is retrieved from Eq. (8), reading

$$\boldsymbol{M}_e = \int_L \begin{bmatrix} \boldsymbol{\Psi} \\ \boldsymbol{\Psi}_{,x} \end{bmatrix}^T \begin{bmatrix} \mathbf{R} & \mathbf{0} \\ \mathbf{0} & \mathbf{Q} \end{bmatrix} \begin{bmatrix} \boldsymbol{\Psi} \\ \boldsymbol{\Psi}_{,x} \end{bmatrix} \mathrm{d}x, \tag{31}$$

with the related GBT modal matrices

$$\mathbf{Q} = \int_S \rho \left( h \overline{\boldsymbol{u}} \overline{\boldsymbol{u}}^T + \frac{h^3}{12} \overline{\boldsymbol{w}} \overline{\boldsymbol{w}}^T \right) \mathrm{d}y, \quad \mathbf{R} = \int_S \rho \left( h (\overline{\boldsymbol{v}} \overline{\boldsymbol{v}}^T + \overline{\boldsymbol{w}} \overline{\boldsymbol{w}}^T) + \frac{h^3}{12} \overline{\boldsymbol{w}}_{,y} \overline{\boldsymbol{w}}_{,y}^T \right) \mathrm{d}y. \tag{32}$$

Finally, in the elastoplastic case recall that the GBT element stiffness matrix is assumed elastic. The incremental load vector stems from Eq. (5) and reads

$$\Delta \boldsymbol{f}_e = \int_\Omega \begin{bmatrix} \boldsymbol{\Psi} \\ \boldsymbol{\Psi}_{,x} \end{bmatrix}^T \begin{bmatrix} \mathbf{0} & \bar{\boldsymbol{v}} & \bar{\boldsymbol{w}} \\ \bar{\boldsymbol{u}} & \mathbf{0} & \mathbf{0} \end{bmatrix} \Delta \boldsymbol{q} \, \mathrm{d}\Omega. \tag{33}$$

All these matrices and vectors are integrated analytically, with the exception of (i) $\boldsymbol{G}_e$, in which case a $3 \times 3$ mid-surface Gauss point grid is adopted in each wall and analytical integration is performed along the thickness, and (ii) the elastoplastic case, where a $3 \times 3 \times 2$ Gauss point grid is adopted (the latter number refers to the through-thickness direction).

## 3. Combining shell and GBT-based finite elements

In the proposed approach, shell finite elements (the most versatile) are used in zones with complex geometries and/or non-linear material behavior, whereas GBT elements are assigned to the prismatic and elastic zones, where just a few deformation modes suffice to obtain accurate results. At a shell-GBT interface, compatibility is enforced through constraint equations of the form

$$\zeta_j \left( U_{kj}^{SFE}(z = 0) - U_{kj}^{GBT}(z = 0) \right) = 0, \tag{34}$$

where $\zeta_j$ are Lagrange multipliers and $U_{kj}^{SFE}$, $U_{kj}^{GBT}$ are the displacements of the mid-surface $(z = 0)$ node $k$ along direction $j$, in the shell and GBT finite elements, respectively. Since only mid-surface nodal displacements are constrained, there is a slight loss of compatibility across the interface, as the shell elements adopt a Reissner-Mindlin description, whereas GBT relies on Kirchhoff's assumption. However, this has little relevance for thin-walled members, where plate-like shearing is negligible. If this effect is important, the shell zones must be extended (this issue will be addressed in the illustrative examples). At the interface, the number of shell DOFs is equal or greater than the GBT one and the constraint equations can be written as

$$\begin{bmatrix} \boldsymbol{\zeta}_c \\ \boldsymbol{\zeta}_d \end{bmatrix}^T \left( \begin{bmatrix} \mathbf{0} & \mathbf{1} & \mathbf{0} \\ \mathbf{0} & \mathbf{0} & \mathbf{1} \end{bmatrix} \begin{bmatrix} \boldsymbol{d}_u^{SFE} \\ \boldsymbol{d}_c^{SFE} \\ \boldsymbol{d}_d^{SFE} \end{bmatrix} - \begin{bmatrix} \mathbf{0} & \boldsymbol{B}_{cc}^{GBT} \\ \mathbf{0} & \boldsymbol{B}_{dc}^{GBT} \end{bmatrix} \begin{bmatrix} \boldsymbol{d}_u^{GBT} \\ \boldsymbol{d}_c^{GBT} \end{bmatrix} \right) = 0, \tag{35}$$

where subscripts $u$, $c$ and $d$ denote DOFs that are, respectively, "unconstrained" (do not appear in the equations), "constrained" (associated to the "linked nodes" in Fig. 3, meaning that $\boldsymbol{B}_{cc}^{GBT}$ is a square and invertible matrix) and "dependent" (pertaining to the "hanging nodes" in Fig. 3). Matrices $\boldsymbol{B}_{ij}^{GBT}$ are calculated by first obtaining the deformation modes with GBTUL and then using Eq. (23) to determine the relevant node displacements, with $z = 0$ and $\boldsymbol{\phi} = \boldsymbol{\Psi} \boldsymbol{d}^{GBT}$. If the axes do not match, a coordinate transformation is necessary.

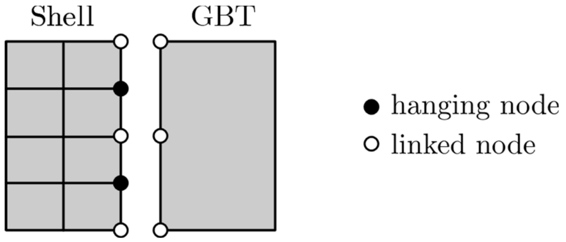

Figure 3: Connection between a shell element assembly and a GBT finite element (a single wall is shown).

Within an incremental-iterative scheme, the global equation system is of the form

$$\begin{bmatrix} \widehat{\boldsymbol{K}}_{uu}^{SFE} & \widehat{\boldsymbol{K}}_{uc}^{SFE} & \widehat{\boldsymbol{K}}_{ud}^{SFE} & \mathbf{0} & \mathbf{0} & \mathbf{0} & \mathbf{0} \\ & \widehat{\boldsymbol{K}}_{cc}^{SFE} & \widehat{\boldsymbol{K}}_{cd}^{SFE} & \mathbf{0} & \mathbf{0} & \mathbf{1} & \mathbf{0} \\ & & \widehat{\boldsymbol{K}}_{dd}^{SFE} & \mathbf{0} & \mathbf{0} & \mathbf{0} & \mathbf{1} \\ & & & \widehat{\boldsymbol{K}}_{uu}^{GBT} & \widehat{\boldsymbol{K}}_{uc}^{GBT} & \mathbf{0} & \mathbf{0} \\ & & & & \widehat{\boldsymbol{K}}_{cc}^{GBT} & -(\boldsymbol{B}_{cc}^{GBT})^T & -(\boldsymbol{B}_{dc}^{GBT})^T \\ & & & & & \mathbf{0} & \mathbf{0} \\ \text{Sym} & & & & & & \mathbf{0} \end{bmatrix} \begin{bmatrix} \Delta\boldsymbol{d}_u^{SFE} \\ \Delta\boldsymbol{d}_c^{SFE} \\ \Delta\boldsymbol{d}_d^{SFE} \\ \Delta\boldsymbol{d}_u^{GBT} \\ \Delta\boldsymbol{d}_c^{GBT} \\ \boldsymbol{\zeta}_c \\ \boldsymbol{\zeta}_d \end{bmatrix} = \begin{bmatrix} \Delta\widehat{\boldsymbol{F}}_u^{SFE} \\ \Delta\widehat{\boldsymbol{F}}_c^{SFE} \\ \Delta\widehat{\boldsymbol{F}}_d^{SFE} \\ \Delta\widehat{\boldsymbol{F}}_u^{GBT} \\ \Delta\widehat{\boldsymbol{F}}_c^{GBT} \\ \mathbf{0} \\ \mathbf{0} \end{bmatrix}, \qquad (36)$$

where the expressions for $\widehat{\boldsymbol{K}}_{ij}$, $\Delta\boldsymbol{d}_i$ and $\Delta\widehat{\boldsymbol{F}}_i$ depend on the analysis type and are discussed next.

### *3.1 Linear static analysis*

In a linear static analysis, the variations $\Delta$ and the "hats" $(\widehat{\ })$ are dropped. Eq. (36) can be simplified by eliminating the Lagrange multipliers and condensing the shell DOFs, leading to a system that only involves the GBT DOFs. Besides leading to a large DOF economy, this procedure is advantageous if a shell macro-element library is built into the code (i.e., matrices $\boldsymbol{K}_{ij}^{SFE}$ are available for several types of member connections) and/or the macro-elements appear at several locations in the model (which typical occurs in steel structures).

In this case, the hanging node DOFs $\boldsymbol{d}_d^{SFE}$ are not constrained, since it is assumed that no severe localized effects occur at the GBT-shell interface. If this assumption is not valid, either these displacements are constrained or the shell zone is extended.

### *3.2 Physically non-linear static analysis*

In a physically non-linear (but geometrically linear) analysis, the "hats" $(\widehat{\ })$ are once more dropped, the tangent stiffness matrices for the shell elements $\boldsymbol{K}_{ij}^{SFE}$ are calculated using $\boldsymbol{C}_{ct}$ and $\Delta\boldsymbol{F}_i$ are replaced by the out-of-balance force vectors $\boldsymbol{g}_i$ ($\boldsymbol{g}_i^{GBT} = \mathbf{0}$ except for the first iteration in each increment). Naturally, the Lagrange multipliers can be eliminated from Eq. (36) and, since the GBT elements are elastic, they are evaluated only once and the corresponding DOFs can be condensed. The shell DOFs could be condensed instead, but this requires performing the related operations in all iterations. In this case $\boldsymbol{d}_d^{SFE}$ needs to be constrained, otherwise stress concentrations appear near the linked nodes and disturb the stress flow through the GBT-shell interface.

To optimize the computational effort, an adaptive refinement strategy is implemented. Initially, all prismatic parts are modeled using GBT (elastic) elements. At each load increment, when convergence is achieved a subroutine checks whether the stresses at the integration points of the GBT elements fall outside the yield surface. If this occurs, the corresponding GBT element is re-meshed with shell elements, its displacements are assigned from the displacements of the previous equilibrium point, and the current increment is recalculated.

### *3.3 Eigenvalue analysis*

In bifurcation or undamped free vibration analyses, $\Delta\widehat{\boldsymbol{F}}_i = \boldsymbol{0}$ in Eq. (36). In the former case one has $\widehat{\boldsymbol{K}}_{ij} = \boldsymbol{K}_{ij} + \boldsymbol{G}_{ij}$, whereas $\widehat{\boldsymbol{K}}_{ij} = \boldsymbol{K}_{ij} - \omega^2\boldsymbol{M}_{ij}$ in the latter case. Once more, the Lagrange multipliers can be eliminated from the equation system. Static condensation is not performed for either the shell or GBT DOFs, since matrices $\widehat{\boldsymbol{K}}_{ij}$ depend on the eigenvalues $\lambda$ and $\omega$, although several strategies to perform such condensation are available (Hitziger et al. 1995).

### *3.4 Dynamic analysis*

The dynamic analysis is performed using the well-known Newmark's method with the parameter values $\beta = 1/4$ and $\gamma = 1/2$. In Eq. (36), $\widehat{\boldsymbol{K}}_{ij} = \boldsymbol{K}_{ij} + c_0\boldsymbol{M}_{ij}$, where $c_0 = 1/(\beta\Delta t^2)$, $\Delta\boldsymbol{d}_i = \boldsymbol{d}_i^{t+\Delta t}$ and

$$\begin{bmatrix} \widehat{\boldsymbol{F}}_u^{SFE} \\ \widehat{\boldsymbol{F}}_c^{SFE} \\ \widehat{\boldsymbol{F}}_d^{SFE} \\ \widehat{\boldsymbol{F}}_u^{GBT} \\ \widehat{\boldsymbol{F}}_c^{GBT} \end{bmatrix} = \begin{bmatrix} \boldsymbol{F}_u^{SFE} \\ \boldsymbol{F}_c^{SFE} \\ \boldsymbol{F}_d^{SFE} \\ \boldsymbol{F}_u^{GBT} \\ \boldsymbol{F}_c^{GBT} \end{bmatrix}_{t+\Delta t} + \begin{bmatrix} \boldsymbol{M}_{uu}^{SFE} & \boldsymbol{M}_{uc}^{SFE} & \boldsymbol{M}_{ud}^{SFE} & \boldsymbol{0} & \boldsymbol{0} \\ & \boldsymbol{M}_{cc}^{SFE} & \boldsymbol{M}_{cd}^{SFE} & \boldsymbol{0} & \boldsymbol{0} \\ & & \boldsymbol{M}_{dd}^{SFE} & \boldsymbol{0} & \boldsymbol{0} \\ & & & \boldsymbol{M}_{uu}^{GBT} & \boldsymbol{M}_{uc}^{GBT} \\ \text{Sym} & & & & \boldsymbol{M}_{cc}^{GBT} \end{bmatrix} \left( c_0 \begin{bmatrix} \boldsymbol{d}_u^{SFE} \\ \boldsymbol{d}_c^{SFE} \\ \boldsymbol{d}_d^{SFE} \\ \boldsymbol{d}_u^{GBT} \\ \boldsymbol{d}_c^{GBT} \end{bmatrix}_t + c_1 \begin{bmatrix} \dot{\boldsymbol{d}}_u^{SFE} \\ \dot{\boldsymbol{d}}_c^{SFE} \\ \dot{\boldsymbol{d}}_d^{SFE} \\ \dot{\boldsymbol{d}}_u^{GBT} \\ \dot{\boldsymbol{d}}_c^{GBT} \end{bmatrix}_t + c_2 \begin{bmatrix} \ddot{\boldsymbol{d}}_u^{SFE} \\ \ddot{\boldsymbol{d}}_c^{SFE} \\ \ddot{\boldsymbol{d}}_d^{SFE} \\ \ddot{\boldsymbol{d}}_u^{GBT} \\ \ddot{\boldsymbol{d}}_c^{GBT} \end{bmatrix}_t \right), \quad (37)$$

with $c_1 = 1/(\beta\Delta t)$ and $c_2 = 1/(2\beta) - 1$. Eq. (36) is solved for each time step and then the accelerations and velocities are updated with

$$\ddot{\boldsymbol{d}}_i^{t+\Delta t} = c_0\left(\boldsymbol{d}_i^{t+\Delta t} - \boldsymbol{d}_i^t\right) - c_1\dot{\boldsymbol{d}}_i^t - c_2\ddot{\boldsymbol{d}}_i^t, \quad (38)$$

$$\dot{\boldsymbol{d}}_i^{t+\Delta t} = \dot{\boldsymbol{d}}_i^t + c_3\ddot{\boldsymbol{d}}_i^t + c_4\ddot{\boldsymbol{d}}_i^{t+\Delta t}, \quad (39)$$

where $c_3 = (1-\gamma)\Delta t$ and $c_4 = \gamma\Delta t$. As in the linear elastic case, the Lagrange multipliers can be eliminated and the shell DOFs can be condensed. All matrices only need to be evaluated at the beginning of the analysis, which leads to a significant economy in terms of computational time.

## **4. Illustrative numerical examples**

In this section a set of numerical examples are presented and discussed, to illustrate the capabilities and potential of the proposed approach. In all examples, the results obtained with the proposed approach are compared with full MITC-4 shell finite element solutions.

### *4.1 Lipped channel cantilever with a tapered segment*

The first example concerns a lipped channel cantilever with a tapered segment having a linearly varying height. Fig. 4(a) shows the beam geometry, material parameters and GBT cross-section discretization adopted. Although 39 deformation modes are obtained with GBTUL, as already mentioned in Section 2.2, only the natural Vlasov (1 to 6) and local-plate modes (7 to 15) are included in the analyses (see Fig. 4(b)).

Three models are considered: (i) a full shell model with 2220 elements, (ii) a less refined GBT-shell model, where only the tapered zone is discretized with shell elements (550 shell elements + 10 GBT elements), and (iii) a refined GBT-shell model where the shell zone is extended 0.25 m into the prismatic part (1100 shell elements + 5 GBT elements).

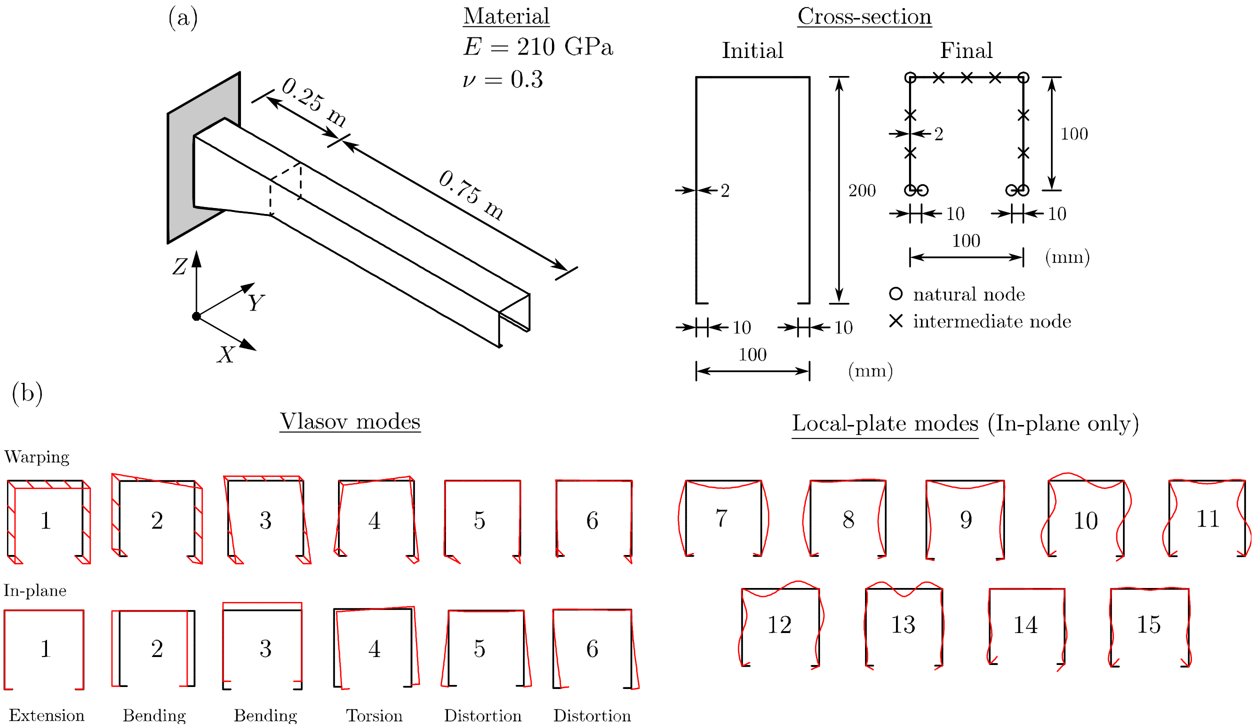

Figure 4: Lipped channel cantilever: (a) geometry, material parameters and GBT cross-section discretization, and (b) first 15 cross-section deformation modes.

Fig. 5(a) displays the linear static results obtained when two point loads are applied at the free end. Both GBT-shell solutions match very accurately the full shell model, as attested by the displacement values of points P1 and P2 in the figure (differences below 1%) and the deformed configurations. The mode amplitude graph shows that minor axis bending (B3) and symmetric distortion (D5) are dominant. Near the interface zone ($X = 0$) several local-plate (LP) modes appear in the less refined GBT-shell model, although they are hardly visible in the corresponding graph. Since the mode amplitude graph of the most refined GBT-shell model is essentially a truncated version of the less refined one, the LP modes naturally disappear. This shows that, as highlighted in Section 3, extending the shell zone dissipates local effects stemming from singularities and, furthermore, makes it possible to use less deformation modes in the GBT-based element — the LP modes could have been discarded in this case.

Fig. 5(b) shows linear stability analysis results, namely the first buckling load (the reference loading now consists of 2 × 1 kN loads) and the corresponding buckling mode for each model. The mode amplitude graphs show that the buckling modes are essentially distortional (D5), although minor-axis bending (B3) also participates along the beam and LP modes appear near the GBT-shell transition zone. The refined GBT-shell model leads to a bifurcation load nearly coincident with that provided by the full shell model (the difference is less than 2%), highlighting once more the benefits of extending the shell macro-element beyond the transition zone (note also that the participations of the LP modes become much smaller). It is worth noting that the buckling loads obtained with the GBT-shell models are slightly lower than that provided by the full shell model, due to the lack of compatibility along the GBT-shell interface.

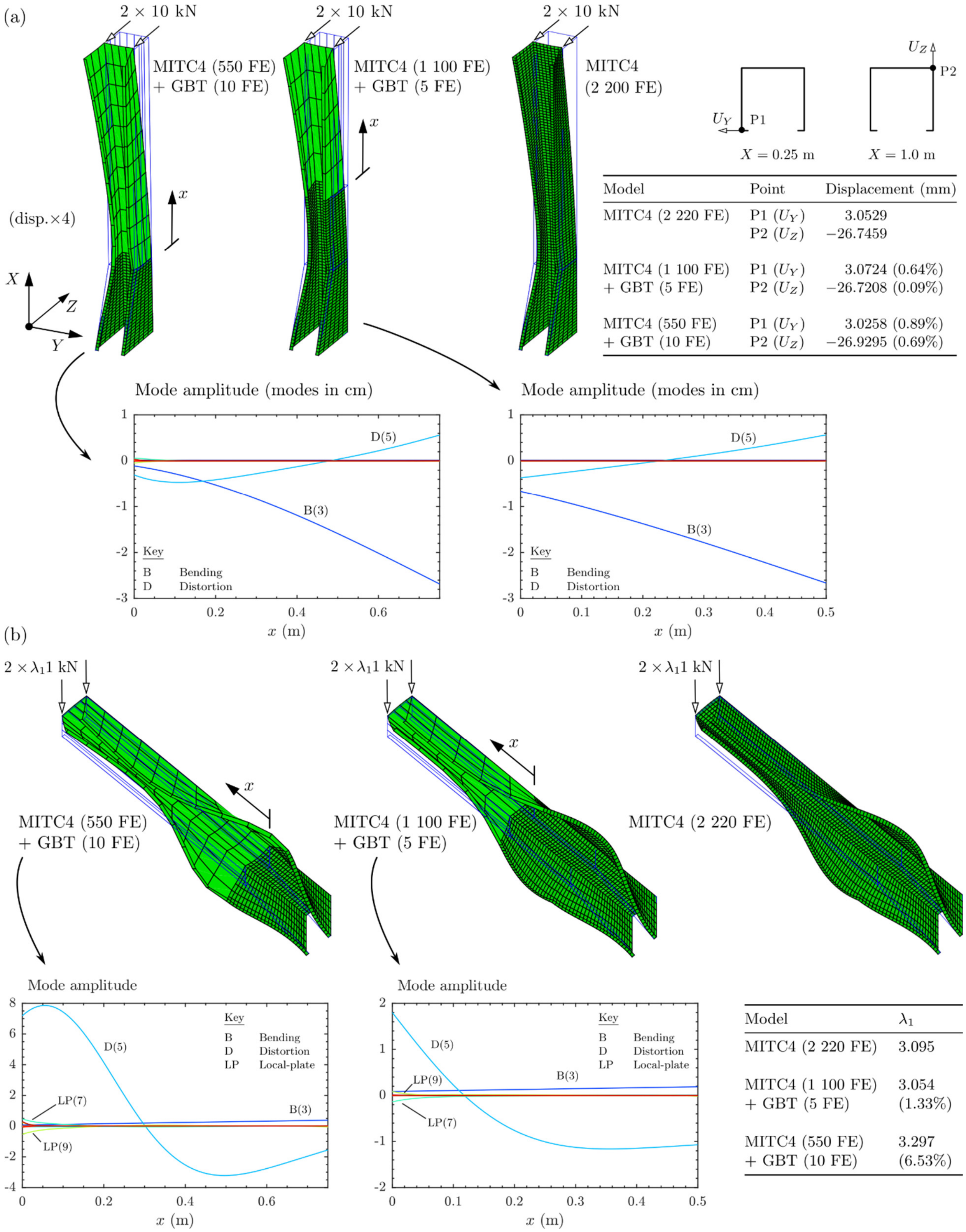

| Model | Point | Displacement (mm) |
|---|---|---|
| MITC4 (2 220 FE) | P1 ($U_Y$)<br>P2 ($U_Z$) | 3.0529<br>−26.7459 |
| MITC4 (1 100 FE)<br>+ GBT (5 FE) | P1 ($U_Y$)<br>P2 ($U_Z$) | 3.0724 (0.64%)<br>−26.7208 (0.09%) |
| MITC4 (550 FE)<br>+ GBT (10 FE) | P1 ($U_Y$)<br>P2 ($U_Z$) | 3.0258 (0.89%)<br>−26.9295 (0.69%) |

| Model | $\lambda_1$ |
|---|---|
| MITC4 (2 220 FE) | 3.095 |
| MITC4 (1 100 FE)<br>+ GBT (5 FE) | 3.054<br>(1.33%) |
| MITC4 (550 FE)<br>+ GBT (10 FE) | 3.297<br>(6.53%) |

Figure 5: Lipped channel cantilever: (a) linear static analysis and (b) bifurcation analysis (first buckling load).

### *4.2 L-shaped cantilevered frame with a tapered joint*

The second example concerns the inverted L-shaped cantilevered frame depicted in Fig. 6(a), having a joint with a complex tapered geometry that significantly influences its structural behavior — therefore, the joint zone must be discretized with shell elements. Except in the linear static and dynamic analyses, two lateral supports are provided at the flanges of the free end cross-section, in order to trigger complex lateral-torsional-local displacements in the joint zone.

The GBT the cross-section discretization adopted involves a single intermediate node in the web, as shown in Fig. 6(a). The resulting deformation modes, included in the GBT finite element, are displayed in Fig. 6(b) and consist of only 4 natural Vlasov and 5 local-plate modes.

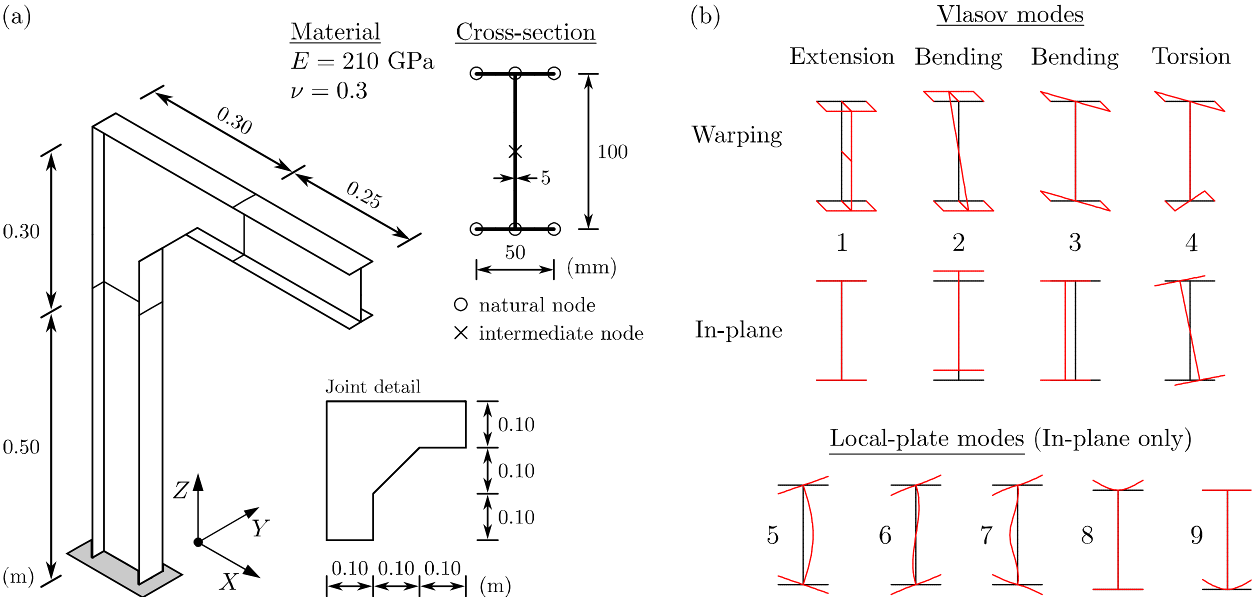

Figure 6: L-shaped frame with a tapered joint: (a) geometry and (b) GBT deformation modes considered.

In all the analyses addressed next two models are compared: (i) a full shell model (2801 elements) and (ii) a GBT-shell model with 1151 shell elements in the joint zone and 10 GBT elements (5 elements in the vertical and horizontal members).

In the linear static analysis, an eccentric 10 kN vertical force is applied at the top flange outstand of the free end cross-section and the results are provided in Fig. 7(a). Despite the complexity of this problem, the GBT-shell model yields a vertical displacement of the point of load application which is virtually identical to that provided by the full shell model (0.17% difference). The GBT mode amplitude graphs displayed in the figure show that the vertical member undergoes essentially in-plane and out-of-plane bending, whereas the horizontal beam exhibits a more complex behavior, involving mostly bending and torsion, but also local effects near the free end, due to the influence of the point load. Note also that, in the horizontal member, the axial extension mode has a constant participation, which indicates that it undergoes a rigid-body horizontal motion.

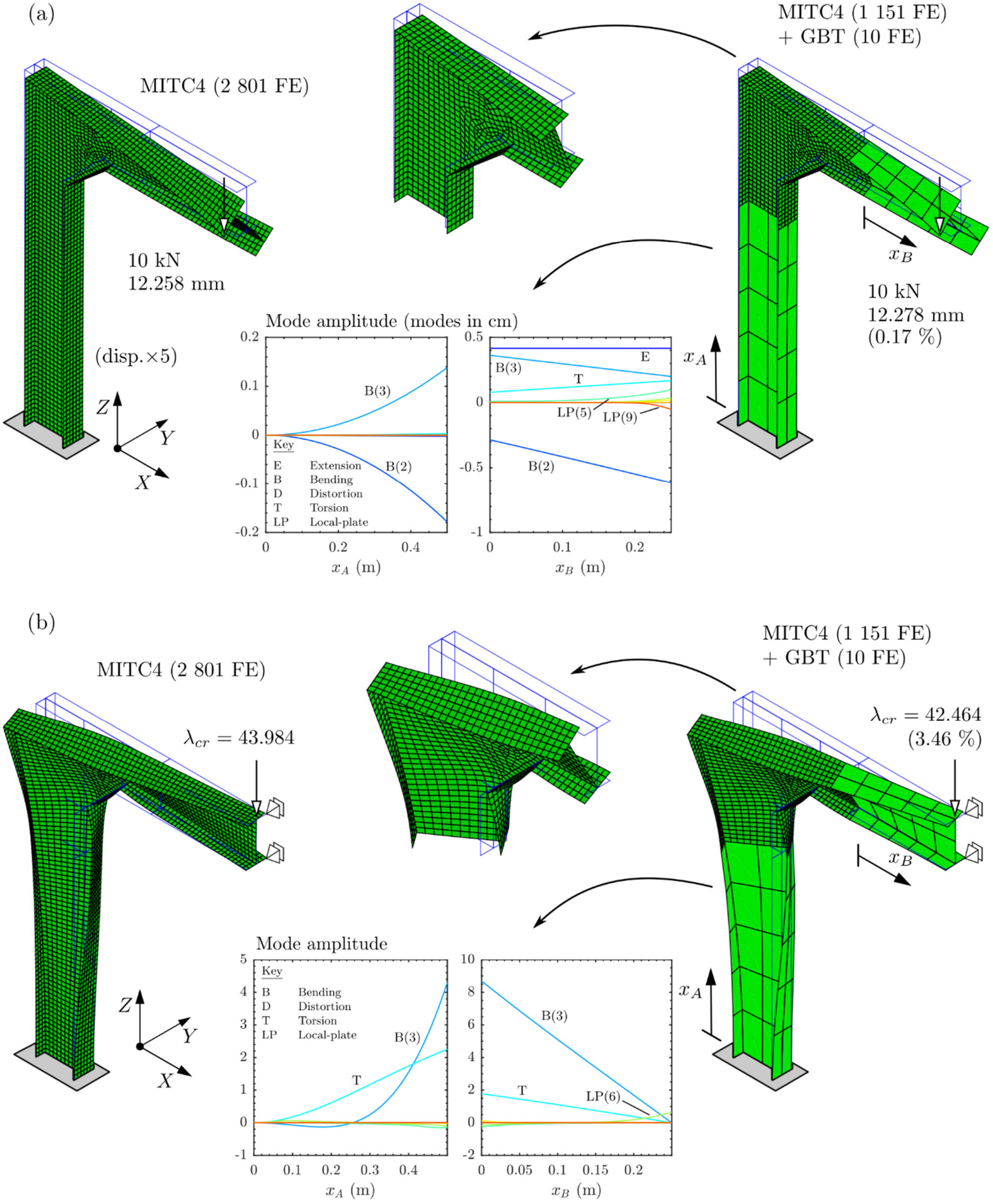

Figure 7: L-shaped cantilevered frame with a tapered joint: (a) linear static analysis and (b) bifurcation analysis.

Consider now a bifurcation analysis of the frame loaded by a single 1 kN load applied at the top web-flange intersection of the free end cross-section — the results are shown in Fig. 7(b). Although the critical buckling mode exhibits a very complex shape at the joint, the GBT-shell model yields excellent results, with a critical load difference with respect to the full shell model of only 3.46%. The mode participation graphs show that the buckling behavior of the prismatic members is almost purely global (i.e., the local-plate modes have almost null participations), thus confirming that the complex behavior is restricted to the joint zone.

Next, adopting $\rho = 2850\ \mathrm{kg/m^3}$, the frame first four natural frequencies and associated vibration modes are determined. Fig. 8 displays these frequencies and modes, obtained with the full shell and the GBT-shell models. A virtually perfect match is observed, with differences in the natural frequencies below 1%. For mode 4 (bottom right) a detail of the joint is shown, to provide a more clear view of its complex deformed shape.

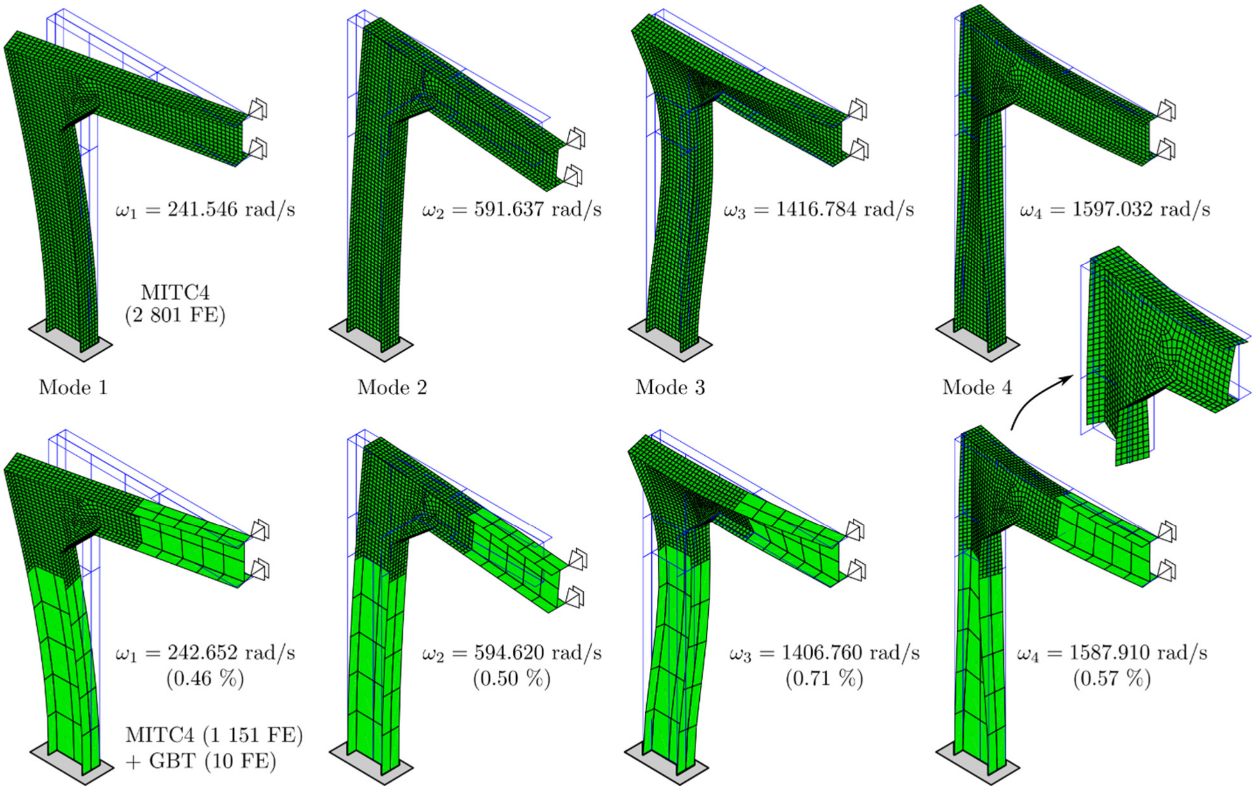

Figure 8: L-shaped cantilevered frame with a tapered joint: first 4 vibration mode shapes and respective frequencies.

Finally, a loading/support case similar to the linear static one is considered (the lateral supports are removed and an eccentric force is applied), but dynamic effects are taken into account through

$$F(t)[\mathrm{kN}] = \begin{cases} 10\sin\left(\dfrac{\pi t}{t_d}\right), & t \leq t_d \\ 0, & t > t_d \end{cases} \tag{40}$$

where $t_d = 0.04$ s. The results obtained with 400 time steps are shown in Fig. 9, which also includes static analysis results for comparison purposes. It is observed that the shell and GBT-shell models provide very similar responses, namely after the load is removed. It is also worth noting that the GBT-shell model runs in half the time of the full shell model.

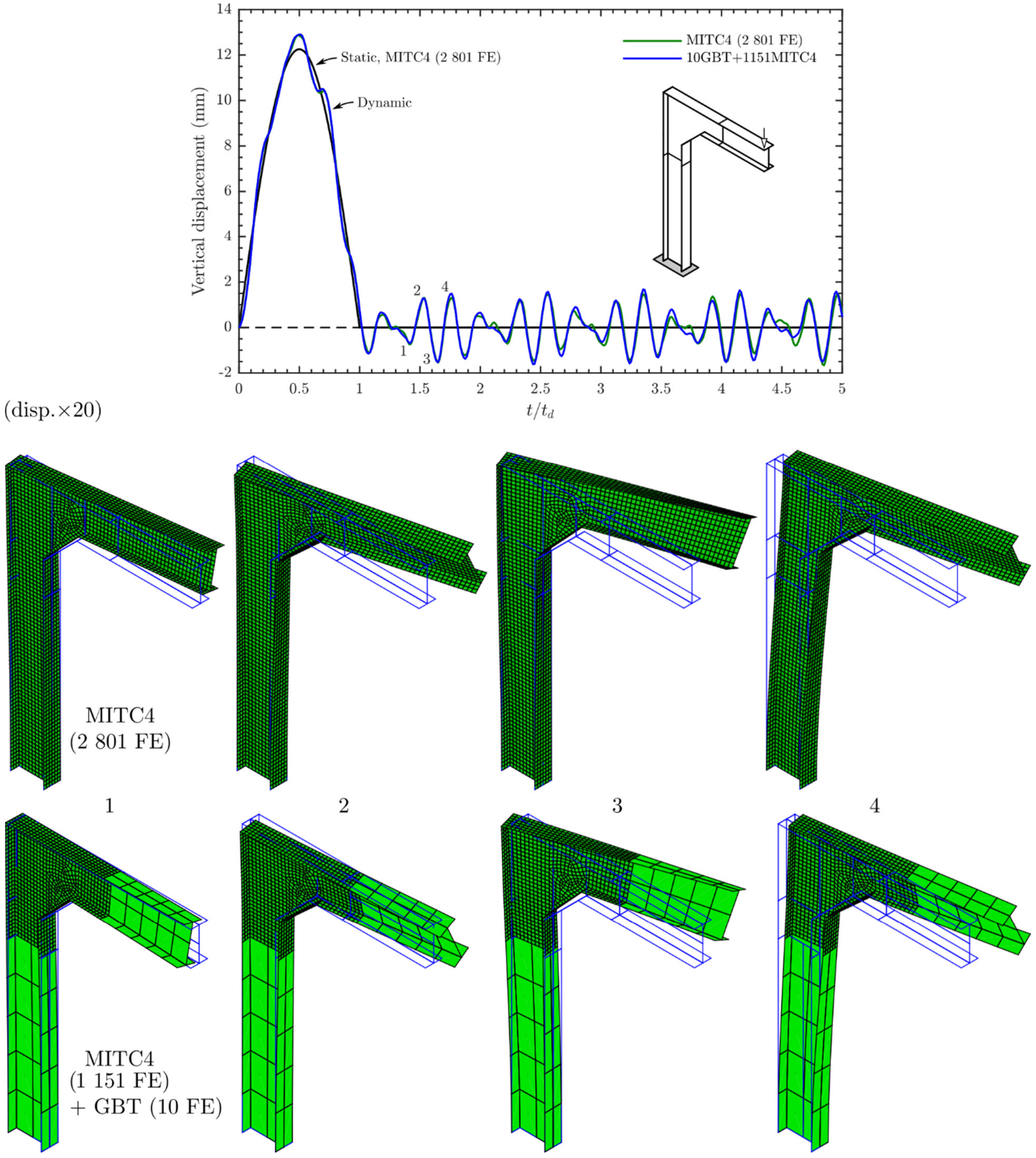

Figure 9: L-shaped cantilevered frame with a tapered joint: dynamic analysis.

### *4.3 Simply supported hat section beam*

This numerical example concerns the physically non-linear (elastoplastic) static analysis of a 1 m long simply supported hat section beam loaded by two forces, applied at the mid-span flange-web corners. Fig. 10 displays (a) the material parameters, beam geometry and loading (advantage was taken of the problem double symmetry), as well as (b) the relevant (symmetric) cross-section deformation modes: extension (E), bending (B) and distortion (D). This example was originally analyzed by Gonçalves & Camotim (2011), using elastoplastic GBT finite elements, and is particularly interesting because significant cross-section distortion occurs along the whole beam length (even in the elastic zones).

Fig. 10 displays the results obtained with the GBT-shell model, adopting the mesh refinement strategy outlined in Section 3.2, and a full shell model. They consist of the (c) load-displacement plot and (d) deformed configurations for several vertical displacements of the load application point, together with the corresponding GBT mode amplitude graphs for the first and last cases. The deformed configurations make it possible to visualize the evolution of the GBT-shell mesh, even if the number of GBT-shell elements for each equilibrium point is also indicated in the graph in Fig. 10(c) (the first point is elastic and is obtained with only 5 equal-length GBT elements).

The load-displacement plot in Fig. 10(c) shows that the GBT-shell approach provides virtually the same results as the full shell model. The number of GBT elements obviously decreases as the loading increases and plasticity spreads, ending up with only two elements for displacements higher than 20 mm. The deformed configurations in Fig. 10(d) provide further evidence of the excellent match, including the evolution of the plastic zones (the yellow color is used when any shell integration point reaches yielding). In particular, the GBT-shell model captures very accurately the cross-section severe distortion and the top flange “bulging” at mid-span, even if slight differences can be detected concerning the extent of the plastic zones — recall that the mesh is refined only if the GBT integration point stresses fall outside the yield surface, a situation that always occurs with a slight “delay” with respect to the full shell model (because the GBT mesh is coarser).

The mode amplitude graphs in Fig. 10(d) show that the distortional mode is always present in the elastic zone and increases as the displacement grows — note the distortion occurring at the GBT-shell interfaces, for the higher displacement values. This demonstrates clearly that it is advantageous to use GBT-based finite elements, since cross-section deformation can play a significant role in the elastic zones.

The computation times can be quite significant in elastoplastic analyses. With respect to the full shell model, the GBT-shell one runs about 320 times faster in the first (elastic) step, since it involves only GBT elements. The differences decrease as plasticity spreads and shell elements are added, with the final step running only 1.6 times faster.

### *4.4 Lipped channel cantilever with two long holes*

Consider now a 2 m long lipped channel cantilever with two 40×180 mm holes, located at the web mid-height and separated horizontally by 40 mm, as shown in Fig. 11(a). A vertical force is applied at the mid-span top flange-lip corner and a physically non-linear (elastoplastic) static analysis is carried out. The relevant GBT cross-section deformation modes are displayed in Fig. 11(b) and included in the GBT finite elements. The point force triggers torsion-bending-distortion, combined with complex local deformation near the load application point, which is “amplified” by the presence of the holes.

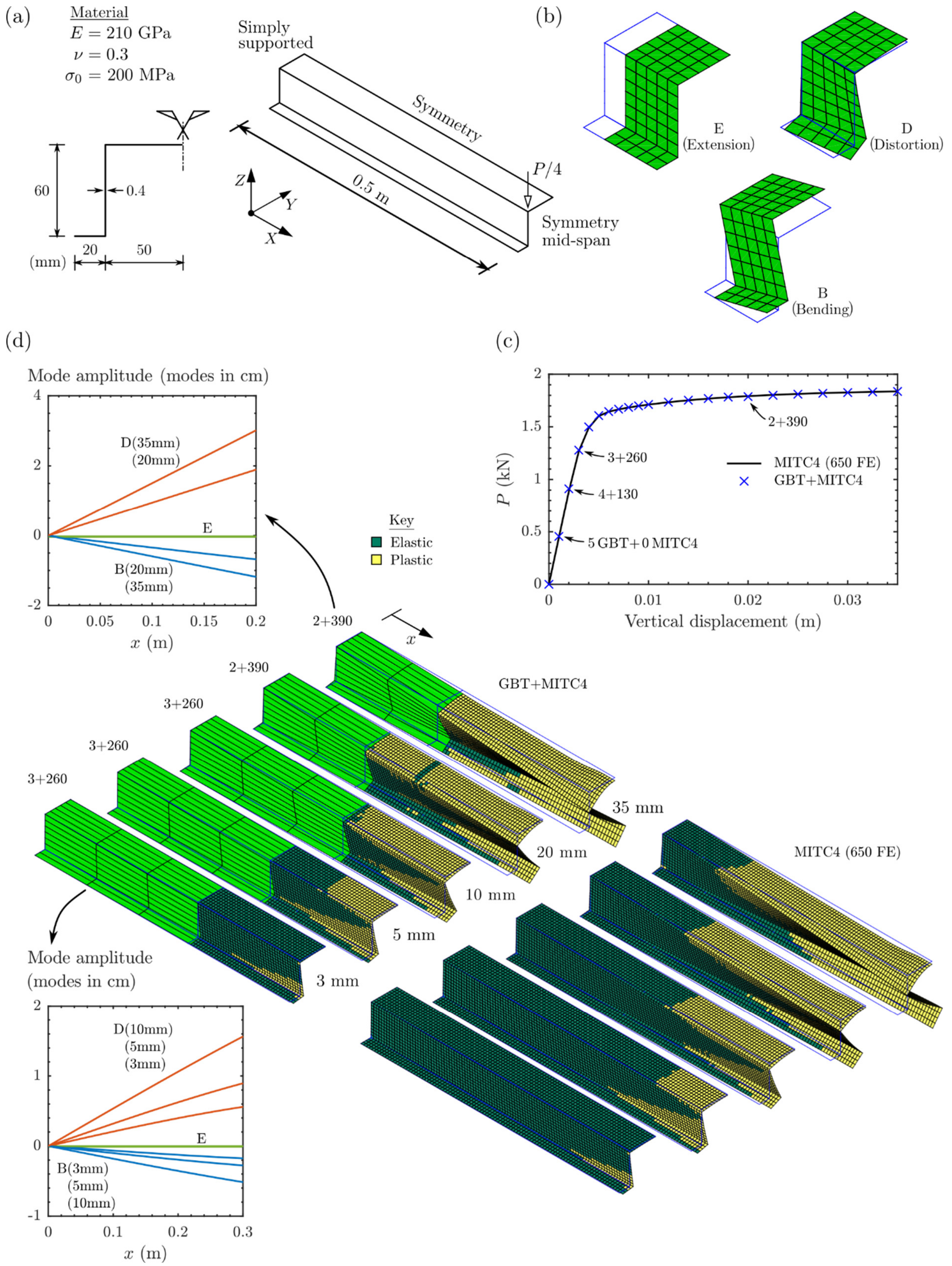

Figure 10: Hat section beam: (a) material parameters, geometry and loading, (b) GBT deformation modes, (c) load-displacement plot, (d) deformed configurations and GBT mode amplitude graphs.

The results obtained with the adaptive GBT-shell and full shell models are provided in Fig. 11, namely (c) the load-displacement plot and the model number for each mesh update point, and (d) the deformed configurations for vertical displacements of the load application point of 20 mm and 150 mm, as well as the corresponding plastic zones and GBT mode amplitude graphs.

The load-displacement graph in Fig. 11(c) shows that the GBT-shell approach provides results that virtually match the full shell model ones. Although 12 equal-length GBT elements are adequate for the first two points of the curve (Model 1), as the loading increases the number of GBT elements decreases. The final model (Model 8) comprises only 4 GBT elements, at the cantilever free end, and 924 shell elements. The deformed configurations displayed in Fig. 11(d) confirm the excellent match obtained, even if slight differences are observed in the plastic zones. However, it is worth mentioning that the GBT-shell model captures very accurately the mid-span cross-section severe distortion and localized deformation of the point of load application. It is also noted that, for a displacement equal to 20 mm, plastic strains are developed not only at the fixed end but also near the point of load application. Increasing further the loading causes a spreading of plasticity between these two cross-sections, until collapse is reached.

The mode amplitude graphs in the bottom of Fig. 11(d) show that both distortional modes (D1 and D2) are present between the fixed end and the load application point, even if major-axis bending (B1) and torsion exhibit the highest amplitudes. Besides major-axis bending and torsion, significant minor-axis bending (B2) also occurs at the free end zone, due to the shift of the centroidal axis caused by plastic strains.

In this example, the GBT-shell model runs 2.6 times faster than the full shell model in the first (elastic) step, since a significant number of shell elements is employed to model the hole zones.

### *4.5 I-section plane frame*

The final numerical example consists of the physically non-linear analysis of the symmetric plane frame shown in Fig. 12(a) subjected to a point load applied at the top of the beam mid-span cross-section. At the load application point, 5 mm thick stiffening plates are provided. Due to symmetry, only half of the frame is analyzed. The purpose of this example is to show that joints developing plastic strains can be easily modeled with the proposed approach.

Since this cross-section does not have Vlasov distortional modes and the loading causes in-plane displacements, the GBT finite element only includes extension and major-axis bending modes (see Fig. 12(b)).

Fig. 12 displays the results obtained with a GBT-shell and a full shell model, namely (c) the load-displacement plot and (d) the deformed configurations and plastic zones for vertical displacements of the point of load application equal to 10 mm and 100 mm, together with the corresponding GBT mode amplitude graphs. Once again, a virtually perfect match between both models is observed throughout the whole load-displacement range considered, even if the number of DOFs is significantly lower in the GBT-shell model (recall that the beam finite elements include only two deformation modes). The deformed configurations show that, throughout the whole loading range

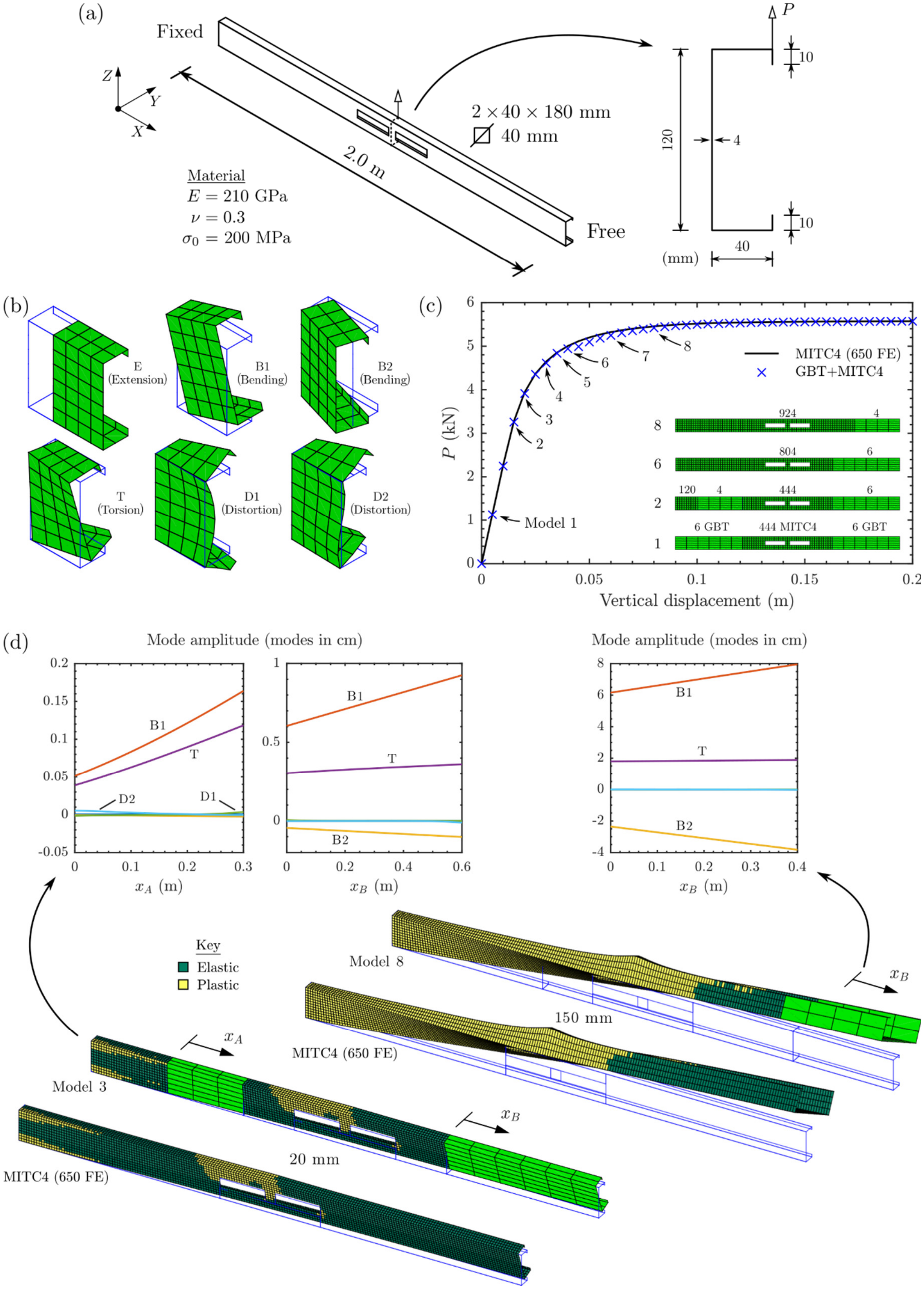

Figure 11: Lipped channel cantilever with two long holes: (a) material parameters, geometry and loading, (b) GBT deformation modes, (c) load-displacement plot and mesh evolution, (d) deformed configurations and mode amplitude graphs.

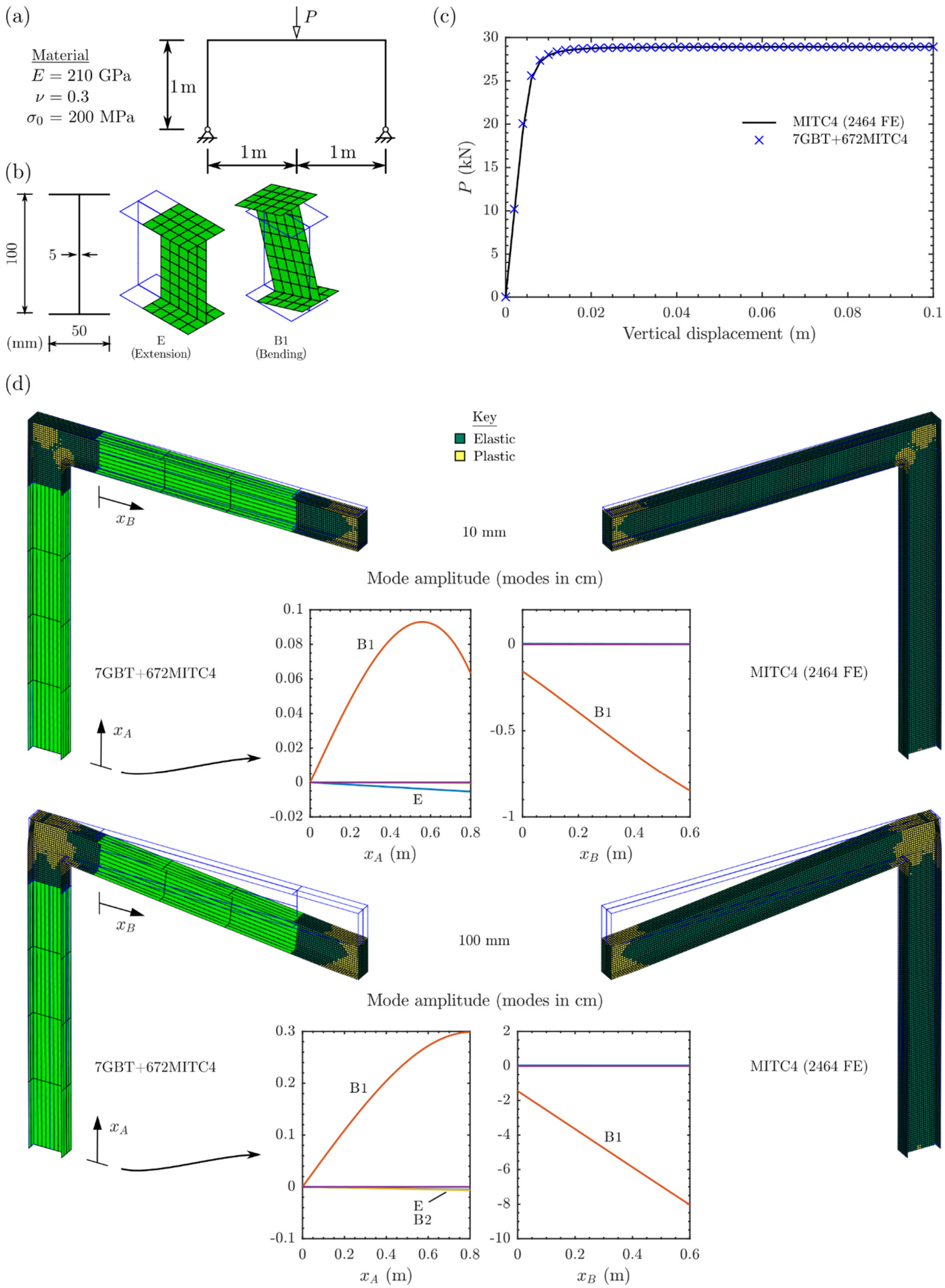

Figure 12: Plane frame: (a) material parameters, geometry and loading, (b) GBT deformation modes, (c) load--displacement plot, (d) deformed configurations and mode amplitude graphs.

considered, the plastic zones are concentrated at the beam mid-span and beam-to-column joints, thus making it unnecessary to perform adaptive mesh refinements. As for the mode amplitude graphs, they confirm that major-axis bending is the dominant mode, but small compressive axial forces (corresponding to negative-slope linear amplitudes of the axial extension mode E) develop in the column and beam.

Concerning the computation times, the GBT-shell model runs about 4 times faster in all steps, since no additional shell elements are necessary throughout the analysis.

## 5. Conclusion

This paper presented a general and efficient approach to analyze thin-walled members with complex geometries and connections, which combines standard shell and GBT-based finite elements. The GBT elements are used to model the prismatic and elastic members, whereas the more complex zones (undergoing plastic straining, having discontinuities, holes, joints, etc.) are handled by means of shell elements. This approach has several significant advantages: (i) the number of deformation modes employed in the GBT elements is greatly reduced (with respect to full GBT analyses), (ii) zones with complex geometries (joints, tapered segments, holes, etc.) can be hadled, (iii) computational efficiency is maximized, since each element type is employed where it is more effective. Moreover, in many types of analysis, either the shell or GBT DOFs can be condensed out of the global equilibrium equation system, thus leading to a very high DOF economy and ensuring fast computation times — the last advantage is particularly important if the full structure has many identical zones.

To illustrate the capabilities and potential of the proposed approach, several numerical examples were presented and discussed, concerning linear (first-order) static, bifurcation (linear stability), undamped free vibration, dynamic and first-order plastic zone analyses. These examples involved tapered segments, holes and frames with complex beam-column assemblies. For validation and comparison purposes, full shell finite element model solutions were provided and an excellent agreement was observed in all cases.

Finally, just two words to mention that the authors are currently investigating the extension of the approach proposed in this work to analyze thin-walled members and structural systems, so that it covers also the large displacement and finite rotation range.

## Acknowledgments

The first author gratefully acknowledges the financial support of FCT (Fundação para a Ciência e a Tecnologia, Portugal), through the doctoral scholarship SFRH/BD/130515/2017.

## References

Basaglia C., Camotim D., Silvestre N. (2008). Global buckling analysis of plane and space thin-walled frames in the context of GBT, *Thin-Walled Structures*, **46**(1), 79-101.

Basaglia C., Camotim D., Silvestre N. (2009). GBT-based local, distortional and global buckling analysis of thin-walled steel frames, *Thin-Walled Structures*, **47**(11), 1246-1264.

Basaglia C., Camotim D., Silvestre N. (2013). Post-buckling analysis of thin-walled steel frames using Generalized Beam Theory (GBT), *Thin-Walled Structures*, **62**(January), 229-242.

Bathe K.J. (1996). *Finite Element Procedures* (1st ed.), Prentice-Hall Inc., New Jersey, USA.

Bathe K.J., Dvorkin E.N. (1985). A four-node plate bending element based on Mindlin/Reissner plate theory and a mixed interpolation, *International Journal for Numerical Methods in Engineering*, **21**(2), 367-383.

Bebiano R., Gonçalves R., Camotim D. (2015). A cross-section analysis procedure to rationalise and automate the performance of GBT-based structural analyses, *Thin-Walled Structures*, **92**(July), 29-47.

Bebiano R., Camotim D., Gonçalves R. (2018). GBTUL 2.0 – a second-generation code for the GBT-based buckling and vibration analysis of thin-walled members, *Thin-Walled Structures*, **124**(March), 235-257.

Cai J., Moen C.D. (2016). Elastic buckling analysis of thin-walled structural members with rectangular holes using Generalized Beam Theory, *Thin-Walled Structures*, **107**(October), 274-286.

Camotim D., Basaglia C. (2013). Buckling analysis of thin-walled steel structures using Generalized Beam Theory (GBT): state-of-the-art report, *Steel Construction*, **6**(2), 117-131.

Gonçalves R., Camotim D. (2004). GBT local and global buckling analysis of aluminium and stainless steel columns, *Computers & Structures*, **82**(17-19), 1473-1484.

Gonçalves R., Camotim D. (2011). Generalized Beam Theory-based finite elements for elastoplastic thin-walled metal members, *Thin-Walled Structures*, **49**(10), 1237-1245.

Gonçalves R., Camotim D. (2012). Geometrically non-linear Generalized Beam Theory for elastoplastic thin-walled metal members, *Thin-Walled Structures*, **51**(February), 121-129.

Gonçalves R., Camotim D. (2017). Improving the efficiency of GBT displacement-based finite elements, *Thin-Walled Structures*, **111**(February), 165-175.

Gonçalves R., Le Grognec P., Camotim D. (2010). GBT-based semi-analytical solutions for the plastic bifurcation of thin-walled members, *International Journal of Solids and Structures*, **47**(1), 34-50.

Gonçalves R., Bebiano R., Camotim D. (2014). On the shear deformation modes in the framework of Generalised Beam Theory, *Thin-Walled Structures*, **84**(November), 325-334.

Hitziger T., Mackens W., Voss H. (1995). A condensation-projection method for generalized eigenvalue problems, *High Performance Computing in Engineering*, vol. 1, H. Power and C.A. Brebbia (eds.), Computational Mechanics Publications, Southampton, 239-282.

Henriques D., Gonçalves R., Camotim D. (2015). A physically non-linear GBT-based finite element for steel and steel-concrete beams including shear lag effects, *Thin-Walled Structures*, **90**(May), 202-215.

Henriques D., Gonçalves R., Camotim D. (2016). GBT-based finite element to assess the buckling behaviour of steel-concrete composite beams, *Thin-Walled Structures*, **107**(October), 207-220.

Henriques D., Gonçalves R., Sousa C., Camotim D. (2020). GBT-based time-dependent analysis of steel-concrete composite beams including shear lag and concrete cracking effects, *Thin-Walled Structures*, **150**(May), paper 106706 (17 pages).

Manta D., Gonçalves R., Camotim D. (2020). Combining shell and GBT-based finite elements: linear and bifurcation analysis, *Thin-Walled Structures*, **152**(July), paper 106665 (14 pages).

Manta D., Gonçalves R., Camotim D. (2021). Combining shell and GBT-based finite elements: plastic analysis with adaptive mesh refinement, *Thin-Walled Structures*, **158**(January), paper 107205 (12 pages).

MATLAB (2010), version 7.10.0 (R2010a), The MathWorks Inc., Massachusetts.

Muresan A.-A., Nedelcu M., Gonçalves R. (2019). GBT-based FE formulation to analyse the buckling behaviour of isotropic conical shells with circular cross-section, *Thin-Walled Structures*, **134**(January), 84-101.

Nedelcu M. (2010). GBT formulation to analyse the behaviour of thin-walled members with variable cross-section, *Thin-Walled Structures*, **48**(8), 629-638.

Nedelcu M. (2011). GBT formulation to analyse the buckling behaviour of isotropic conical shells, *Thin-Walled Structures*, **49**(7), 812-818.

Peres N., Gonçalves R., Camotim D. (2016). First-order Generalised Beam Theory for curved thin-walled members with circular axis, *Thin-Walled Structures*, **107**(October), 345-361.

Peres N., Gonçalves R., Camotim D. (2018). GBT-based cross-section deformation modes for curved thin-walled members with circular axis, *Thin-Walled Structures*, **127**(June), 769-780.

Schardt R. (1996). Eine Erweiterung der Technischen Biegetheorie zur Berechnung prismatischer Faltwerke, *Stahlbau*, **35**(6), 161-171. (German)

Schardt R. (1989). *Verallgemeinerte Technische Biegetheorie*, Springer Verlag, Berlin. (German)

Ritto-Corrêa M., Camotim D. (2001). Integration algorithm for J2 elastoplasticity under arbitrary mixed stress-strain control, *International Journal for Numerical Methods in Engineering*, **50**(5), 1213-1232.

Simo J., Taylor R. (1985). Consistent tangent operators for rate-independent elastoplasticity, *Computer Methods in Applied Mechanics and Engineering*, **48**(1), 101-118.